Nonlinear Dyn (2025) 113:6141–6156
https://doi.org/10.1007/s11071-024-10703-x

RESEARCH

Amplitude death in ring-coupled network with asymmetric thermoacoustic oscillators and nonlocal time-delay interactions

Liheng Zheng · Yu Liao · Kyu Tae Kim · Jie Zhou · Yu Guan

Received: 12 July 2024 / Accepted: 21 November 2024 / Published online: 2 December 2024

Abstract This numerical study examines the pressure amplitude distribution, focusing on amplitude death, in a ring-coupled network of nonlocally coupled asymmetric thermoacoustic oscillators. Each decoupled self-excited thermoacoustic oscillator is modeled using the classical Rijke tube model. We investigate three configurations with asymmetric thermoacoustic oscillators: localized asymmetry, side-by-side asymmetry, and alternating asymmetry. Asymmetries are introduced through frequency detuning and heater power mismatching. Our study reveals that the configuration with alternating asymmetry induces the largest region of amplitude death compared to the other two configurations, where all originally self-excited oscillators become quenched in the network. The remaining energy of oscillations often concentrates at the two ends of the axis of symmetry. The region of amplitude death generally increases with the number of thermoacoustic oscillators and remains unchanged when the number of oscillators is sufficiently large ($n = 8$). The variation of the global average pressure amplitude predicted by the proposed model qualitatively agrees with previous experimental observations. In summary, we conclude: (1) reduced-order models developed from a dynamical system approach can provide a qualitative prediction of the system's pressure amplitude distribution, potentially offering useful information for avoiding operating parameters that lead to high-amplitude thermoacoustic oscillations in multi-combustor systems; and (2) introducing asymmetries into a ring-coupled network can potentially be leveraged to weaken self-excited oscillations in multi-combustor systems globally.

Keywords Amplitude death · Coupling-induced dynamics · Reduced-order model · Thermoacoustic instability

L. Zheng · Y. Liao · Y. Guan (✉)
Department of Aeronautical and Aviation Engineering, The Hong Kong Polytechnic University, Kowloon, Hong Kong
e-mail: yu.guan@polyu.edu.hk

L. Zheng · J. Zhou (✉)
School of Aeronautics, Northwestern Polytechnical University, Xi'an 710072, China
e-mail: jiezhou@nwpu.edu.cn

K. T. Kim
Department of Aerospace Engineering, Korea Advanced Institute of Science and Technology, Daejeon 34141, Republic of Korea

1 Introduction

Thermoacoustic instability, arising from the feedback coupling between unsteady flames and acoustic waves, remains a significant problem in various combustors despite numerous control strategies developed over the years to mitigate it [1–3]. This instability can lead to undesirable flow oscillations and unsteady flame dynamics, making the overall combustion system less efficient and causing catastrophic structural damage to components [4–6]. Can-annular combustors, com-

monly seen in heavy-duty gas turbines, are characterized by a unique type of thermoacoustic instability [7,8]. The properties of this instability are influenced by the acoustic communication induced by the gap between cans and the turbine entry, as well as the acoustic-flame interaction in each individual can [9–11]. When each unstable can is treated as a self-excited thermoacoustic oscillator (TO), the complex collective dynamics observed in such a can-annular combustor can be investigated as coupling-induced dynamics in a network. In this context, the desirable system state of such a network is the global suppression of oscillations. Amplitude death (AD) is a phenomenon where interactions among oscillators stabilize them to a state of global suppression of oscillations [12]. Studying AD in a network of coupled TOs could, therefore, potentially offer valuable insights for controlling undesirable self-excited thermoacoustic oscillations in can-annular combustors.

AD has been reported in various networks consisting of multiple coupled oscillators, including an aeroelastic system of airfoils coupled with springs in the presence of axial flows, [13], a laser system with dual-wavelength optical sources [14], and a network consisting of four coupled candle flames [15]. AD can be achieved through two primary mechanisms: time-delay coupling [16–19] and the mismatch of oscillators' properties [20–23]. Time-delay interactions reflect the time cost of transportation of mass, energy, and information in real situations. Mismatched systems are commonly found in nature since it is rare for all oscillators to be identical. Therefore, these two effects are often taken into consideration in research [23,24]. Even with weak coupling strength, AD can still be achieved by finely tuning frequency mismatches and delay times [23]. This sheds light on achieving AD in industrial combustors where thermoacoustic oscillations are often weakly coupled. Other effects relating to network dynamics are network topology and the number of oscillators, which are also attractive subjects for AD study [25–27]. It was found that random shortcuts can eliminate AD observed in the network [25]. Interestingly, in a small-scale ring network, if an oscillator is coupled with no more than one other oscillator beyond its nearest neighbors, having an odd number of total oscillators will result in a larger AD region [27].

AD has also been reported in the network consisting of multiple coupled TOs. For example, AD was achieved in two thermoacoustic engines coupled with two connecting tubes, which were modeled to represent dissipative coupling and time-delay coupling in a low-order model, respectively [28]. It was found that the simultaneous action of two couplings is more capable of annihilating oscillation. In addition to the network consisting of periodic TOs, AD was also achieved for two coupled chaotic TOs [29]. Unique dynamic behaviors such as complete chaos synchronization and on-off intermittent phenomena emerged in such a chaotic system. AD was possibly achieved even with a significantly smaller connecting tube diameter (i.e., much weaker coupling strength) when multiple time-delay couplings were introduced by connecting two thermoacoustic engines with multiple connecting tubes [30]. Together with the aforementioned study [23], this again implies the feasibility of achieving AD in industrial combustors where the acoustic communication could be weak between coupled TOs [31,32]. Partial AD also exists in TOs. It was demonstrated in two electrical-heater-driven Rijke tubes coupled via a connecting tube, where only one of the two self-excited TOs was quenched [33]. AD can be achieved not only in non-reacting flows but also in reacting flows. For example, AD was achieved in two laminar Rijke tubes coupled with two connecting tubes [34]. Both complete and partial AD states were also achieved in two lean-premixed turbulent combustors mutually coupled with a cross-talk tube [35,36]. However, as the number of TOs increased, AD was no longer observed. For example, AD was not found in a ring-coupled network consisting of four adjacently coupled turbulent TOs, although other rich dynamics such as in-phase/anti-phase synchronization, desynchronization, and weak chimeras were reported [37,38]. Recent numerical studies using low-order modeling revealed that the coupling strength (i.e., the diameter of the coupling tube) might not be large enough to induce AD [39,40]. However, previous studies have demonstrated the possibility of AD emerging in other systems with many TOs. For instance, AD has been identified in very large floating structures consisting of several modules coupled by flexible connectors [41], suggesting that AD can indeed manifest itself in complex systems and become a key factor in evaluating global dynamic stability performance [42]. Therefore, we aim to unravel the mechanism of achieving AD in a ring-coupled network consisting of many self-excited TOs.

In this study, we aim to explore how (1) the coupling condition between TOs, (2) the number of TOs, and

(3) the asymmetries in the properties of TOs affect the emergence of AD in a ring-coupled network consisting of many self-excited TOs (up to 16 TOs). We study these three aspects for the following reasons.

First, the acoustic communication between cans plays a pivotal role in determining collective dynamics in can-annular combustors. For example, Buschmann et al. [10] studied asymmetric coupling in a can-annular combustor consisting of eight cans and revealed that even weak coupling between cans can influence the frequency and modal structure. Several recent numerical studies have also improved the modeling of acoustic communication between cans, including considering aeroacoustic coupling [43] and can reflection coefficients [44]. Given the facts that (i) the propagation of sound waves between TOs can cause reflections due to sudden changes in cross-sectional area, and (ii) the finite speed of sound introduces additional delay times for interactions between more distant TOs, we propose a nonlocal yet evanescent time-delay coupling condition to dynamically model the interactions between coupled TOs. This raises our first research question: Can the network model with the nonlocal time-delay coupling qualitatively predict the amplitude distribution observed in experiments [45–47]?

Second, in many can-annular combustors, there are often many coupled cans (typically 8 to 16). However, many existing studies have often focused on systems consisting of fewer cans (e.g., four cans [45]). This raises our second research question: How do the system's collective dynamics, particularly AD, change across a large range of TOs (up to 16)?

Third, both global and local asymmetries in the properties of TOs have been found to greatly influence collective dynamics in can-annular combustors [9,46]. We introduce three configurations of asymmetries: localized asymmetry, "side-by-side" asymmetry, and adjacent asymmetry, and raise our third research question: How do asymmetries in the properties of TOs affect collective dynamics in this ring-coupled network? Will any type of asymmetry promote the emergence of AD in the network?

To answer these research questions, we first built a ring-coupled network model consisting of TOs using the reduced-order Rijke tube model (Sect. 2). We then comprehensively investigated the influence of asymmetries in the properties of TOs, including frequency detuning and heater power mismatching, on AD in networks with different numbers of TOs (Sect. 3). We qualitatively compared the results obtained from our model with experimental data for 4-can and 5-can combustors in terms of the amplitude distribution (Sect. 3.3). Finally, we conclude this numerical study by discussing the limitations and practical implications of our findings (Sect. 4).

2 Nonlocal ring-coupled TOs

In this study, we use the classical Rijke tube model [48] to model the self-excited TO, which was used to study nonlinear dynamics in thermoacoustic systems before [49–53]. When considering the one-dimensional acoustic field in a duct with both open-ended boundary conditions, negligible mean flow, and mean temperature variation across the tube, as well as the absence of natural convection, the linearized momentum and energy equations can be derived as follows:

$$\tilde{\rho}\frac{\partial \tilde{u}'}{\partial \tilde{t}} + \frac{\partial \tilde{p}'}{\partial \tilde{x}} = 0, \tag{1}$$

$$\frac{\partial \tilde{p}'}{\partial \tilde{t}} + \gamma \overline{p}\frac{\partial \tilde{u}'}{\partial \tilde{x}} + \zeta \tilde{p}' = (\gamma - 1)\dot{\tilde{Q}}'\delta(\tilde{x} - \tilde{x}_f), \tag{2}$$

where the superscript $\tilde{(\,)}$ denotes dimensional variables, and the superscript $(\,)'$ denotes fluctuating variables. Here, $\tilde{t}$, $\tilde{u}$, and $\tilde{p}$ are the time, acoustic velocity, and acoustic pressure in the duct, respectively. $\tilde{x}$ is the distance along the inlet of the duct, and $\tilde{x}_f$ is the location of the heat source. We choose $\tilde{x}_f = 0.25$ since this is the optimum location to generate self-excited thermoacoustic oscillations in the duct. $\tilde{\rho}$ is the density, γ is the specific heat ratio, ζ is the damping coefficient, and $\dot{\tilde{Q}}'$ is the heat release rate in the duct. $\delta(\,)$ is the Dirac function, which is used to introduce the compactness of the heat source.

The boundary condition at $\tilde{x} = L$ (where L is the length of the duct) is $\tilde{p}'|_{\tilde{x}=L} = 0$, indicating that the pressure fluctuation $\tilde{p}'$ at both ends of the duct is negligible. To better analyze the system, the variables in Eqs. (1) and (2) are nondimensionalized as follows:

$$\begin{aligned} x &= \frac{\tilde{x}}{L},\ t = \frac{\tilde{t}c_0}{L},\ u' = \frac{\tilde{u}'}{u_0}, \\ p' &= \frac{\tilde{p}'}{\overline{p}},\ \dot{Q}' = \frac{\dot{\tilde{Q}}'}{c_0\overline{p}},\ M = \frac{u_0}{c_0}, \end{aligned} \tag{3}$$

where c_0, u_0, $\overline{p}$ and M are the sound speed, the mean flow velocity, pressure, and Mach number, respectively.

Equations (1) and (2) can then be transformed into their non-dimensional forms using Eq. (3):

$$\gamma M \frac{\partial u'}{\partial t} + \frac{\partial p'}{\partial x} = 0, \tag{4}$$

$$\frac{\partial p'}{\partial t} + \gamma M \frac{\partial u'}{\partial x} + \zeta p' = (\gamma - 1)\dot{Q}'\delta(x - x_f). \tag{5}$$

The heat release, $\dot{Q}'$, is modelled using a modified form of King's law, proposed by Heckl [54]. The selection of this model involves a trade-off between its simplicity and effectiveness, which facilitate the capturing of key phenomena, and its empirical nature, which introduces certain limitations, such as discontinuities. Nevertheless, this model incorporates the two most influential terms found in more advanced heat release models: the time lag and the nonlinear damping caused by acoustic radiation. In addition, this model has been widely adopted in similar previous studies focusing more on nonlinear dynamics in thermoacoustic systems, as discussed in Sect. 1. Therefore, it is an acceptable choice for establishing the baseline framework for investigating ring-coupled thermoacoustic networks. The model is expressed as follows:

$$\begin{aligned}\dot{Q}'(t) =& \frac{2L_h(T_h - \overline{T})}{S\sqrt{3}c_0\overline{p}}\sqrt{\pi\lambda c_v u_0 \overline{\rho} r_h} \\ &\times \left[\sqrt{\left|\frac{1}{3} + u_f'(t - \tau_t)\right|} - \sqrt{\frac{1}{3}}\right],\end{aligned} \tag{6}$$

where L_h, T_h and r_h are the length, temperature and heater wire radius, respectively. $\overline{T}$ is the average temperature of surrounding air. S is the cross-sectional area of the duct. λ and c_v are the thermal conductivity and constant-volume specific heat, respectively. τ_t is the response time lag between the start of the heat source's response to the acoustic velocity perturbation, u'_f, due to the thermal inertia of the heater wire.

To solve Eqs. (4) and (5), we utilize the Galerkin method to transform these partial differential equations into a set of discrete ordinary differential equations. To accomplish this, we express the dimensionless velocity u' and pressure oscillation p' as orthogonal bases that match the boundary conditions [55,56].

$$u' = \sum_{j=1}^{N} \eta_j \cos(j\pi x), \tag{7}$$

$$p' = -\sum_{j=1}^{N} \dot{\eta}_j \frac{\gamma M}{j\pi} \sin(j\pi x), \tag{8}$$

where η_j and $\dot{\eta_j}$ are the time-dependent amplitudes of the acoustic velocity oscillation u' and acoustic pressure oscillation p' for the jth Galerkin mode, respectively. The parameter N is the total number of Galerkin modes. We choose $N = 10$ following previous studies [56], as additional modes yield only marginal enhancements in modeling solutions.

Combining Eqs. (4)–(8), we derive the set of ODEs that describe the behavior of a single TO:

$$\frac{\mathrm{d}\eta_j}{\mathrm{d}t} = \dot{\eta}_j, \tag{9}$$

$$\begin{aligned}&\frac{\mathrm{d}\dot{\eta}_j}{\mathrm{d}t} + 2\zeta_j\omega_j\dot{\eta}_j + \omega_j^2\eta_j \\ &= -j\pi K\left[\sqrt{\left|\frac{1}{3} + u_f'(t - \tau_t)\right|} - \sqrt{\frac{1}{3}}\right]\sin(j\pi x_f),\end{aligned} \tag{10}$$

where $\omega_j = j\pi$ is the angular frequency of the j^{th} Galerkin mode and ζ_j is the acoustic damping, which is developed by Matveev [57]:

$$\zeta_j = \frac{1}{2\pi}\left[c_1\frac{\omega_j}{\omega_1} + c_2\sqrt{\frac{\omega_1}{\omega_j}}\right], \tag{11}$$

where c_1 and c_2 are the damping coefficient. In this study, we choose the parameters of this Rijke tube model to be: $c_1 = 0.1$, $c_2 = 0.06$, $\tau_t = 0.2$, $M = 0.01$, and $\tilde{x_f} = 0.25$, while varying the nondimensional heater power K. K is defined as follows:

$$K = 4(\gamma - 1)\frac{2L_h(T_h - \overline{T})}{M\gamma S\sqrt{3}c_0\overline{p}}\sqrt{\pi\lambda c_v u_0\overline{\rho} r_h}. \tag{12}$$

In this study, we propose a nonlocal time-delay coupling model for describing the amplitude distribution in multiple ring-coupled TOs, as illustrated in Fig. 1. This model maintains the original dissipative coupling but modifies the time-delay coupling such that the interaction from i^{th} TO now propagates to further TOs with a transmission loss. The modified ODEs [Eqs. (9) and

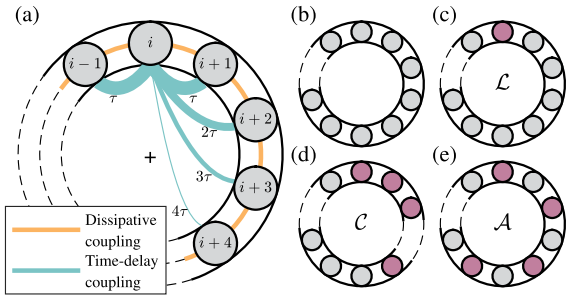

Fig. 1 **a** The coupling interaction of i^{th} thermoacoustic oscillator (TO) in the multiple-coupled network. Dissipative coupling occurs between adjacent TOs and the time-delay coupling occurs between two arbitrary TOs. The line width of time-delay coupling represents the overall nonlocal coupling strength. **b**–**e** The configurations of the ring-coupled network, which are the uniform case, the localized asymmetric case ($\mathcal{L}$ case), the 'side-by-side' case ($\mathcal{C}$ case), and the alternating case ($\mathcal{A}$ case), respectively

(10)], for the i^{th} TO take the following form:

$$\begin{aligned}
&\ddot{\eta}_j + 2\zeta_j\omega_j\dot{\eta}_j + \omega_j^2\eta_j \\
&\quad = -j\pi K\left[\sqrt{\left|\frac{1}{3}+u_f{}'(t-\tau_t)\right|}-\sqrt{\frac{1}{3}}\right]\sin(j\pi x_f) \\
&\qquad + \underbrace{\sum_{p=1}^{n} k_\tau(1-c_{\text{loss}})^{p-1}((\dot{\eta}_j^{i+p}+\dot{\eta}_j^{i-p})(t-p\tau)-2\dot{\eta}_j^{i}(t))}_{\text{Nonlocal time-delay coupling}} \\
&\qquad + \underbrace{k_d(\dot{\eta}_j^{i+1}+\dot{\eta}_j^{i-1}-2\dot{\eta}_j^{i})}_{\text{Dissipative coupling}},
\end{aligned} \tag{13}$$

where the superscript $(\,)^i$ denotes the parameters associated with the i^{th} TO, while superscripts $(\,)^{i+p}$ and $(\,)^{i-p}$ represent nonlocal coupled TOs, and superscripts $i+1$ and $i-1$ denote the immediately adjacent TOs. Here, p signifies the distance between two nonlocally coupled TOs, with $p=1$ indicating adjacent coupling and $p>1$ denoting nonlocal coupling. The term c_{loss} ($0 \leqslant c_{\text{loss}} \leqslant 1$), which decays exponentially with an increase in p, represents the transmission loss between TOs. We validated our model and numerical configuration by repeating the same bifurcation analysis as was done in [58], with the results presented in Appendix A. In this study, we adopt the nonlocal coupling network model and perform numerical simulations to investigate the influences of various parameters on the emergence of AD. These parameters include time-delay coupling strength k_τ (dissipative coupling strength is fixed at $k_d = 0.2$), time delay between coupled TOs (τ), nondimensional heater power (K), the number of TOs (n), the frequency detuning ratio (δ_ω), and heater power mismatching ratio (δ_K). To prevent noise-induced dynamics, we keep our decoupled self-excited TO sufficiently away from the Hopf point at $K = 0.64$ and then vary K across a broad range. We consider n ranging from 4 to 8 with an additional case of $n = 16$ included for a convergence study. It is noted that n has limited effect on the oscillation amplitude when $n > 20$ [17,59].

3 Results and discussions

In the following sections, we aim to answer three research questions raised in Sect. 1 by performing numerical simulations of the low-order network model proposed in Sect. 2.

3.1 Nonlocal coupling effect

To quantify the global variation of all TOs' pressure amplitudes in a network under different coupling conditions, we define $\overline{A} \equiv 1/n \sum_{i=1}^{n} A_i$. Here, the normalized pressure amplitude of the i^{th} TO, out of a total of n TOs, is given by $A_i = p'_{i,\text{rms}}/p'_{0,\text{rms}}$ ($i = 1, 2, ..., n$), where subscripts $(\,)_{\text{rms}}$, $(\,)_i$, and $(\,)_0$ denote the root-mean-square value of p', the value of i^{th} nonlocally coupled TO, and the decoupled base TO, respectively. The properties of the decoupled base TO are presented in Appendix A. We then determine AD as occurring when $A_i \leqslant 0.01$ for all TOs.

We first compare the results of adjacent coupling with those of nonlocal coupling for different TO numbers. The adjacent coupling can be expressed by setting $c_{\text{loss}} = 1$, indicating that sound waves are impeded from passing through an adjacent TO and thereby cannot propagate further. Conversely, $c_{\text{loss}} = 0$ denotes global coupling with no transmission loss. Therefore, we can determine how "far" acoustic waves can propagate across coupled TOs in the network by manipulating the value of c_{loss}. When TOs are adjacently coupled, the $\overline{A}$ distribution in the parameter space defined by τ and k_τ remains largely consistent across different n, as

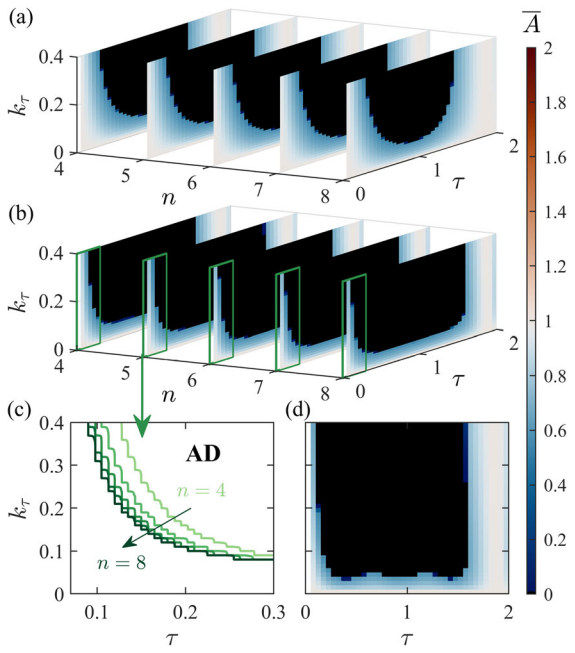

Fig. 2 Contour maps of the global average of the normalized pressure amplitude of TOs (i.e., $\overline{A}$) for **a** adjacent coupling case $c_{\text{loss}} = 1$ and **b** nonlocal coupling case $c_{\text{loss}} = 0.5$. Panel **c** shows a magnified view of the AD boundary enclosed by a green box in (**b**). Panel **d** shows the contour map of $\overline{A}$ for the global coupling case with $c_{\text{loss}} = 0$ and $n = 4$. The heater power is $K = 1.4$ and the dissipative coupling strength is $k_d = 0.2$

shown in Fig. 2a. The size of the AD region therefore does not change when n changes. By contrast, when TOs nonlocally coupled ($c_{\text{loss}} = 0.5$), the size of the AD region enlarges when n increases because of the amplified coupling effect, although the $\overline{A}$ distributions are generally similar across different n, as shown in Figs. 2b and 2c. Nonetheless, this amplified coupling effect is confined to a finite size of the network; when the number of TOs exceeds 20, this enhanced coupling effect scarcely affects the system's collective behavior [17,59]. We then further examine the results of global coupling when $c_{\text{loss}} = 0$, as shown in Fig. 2d. We find that the AD region is further enlarged, facilitating the emergence of AD particularly for $k_\tau \leqslant 0.2$ and specific time delays ($\tau = \pi/2\omega$ and $\tau = 3\pi/2\omega$, ω is the natural frequency of decoupled base TO in Appendix A).

3.2 Effect of asymmetries in the network

Here, we investigate three configurations with asymmetric TOs: the localized asymmetric case (denoted as the $\mathcal{L}$ case), the 'side-by-side' asymmetric case (denoted as the $\mathcal{C}$ case), and the adjacent asymmetric case (denoted as the $\mathcal{A}$ case), as illustrated in Fig. 1(b–e). We also include a uniform configuration for comparison, where all TOs share the same natural frequency ω and heater power K. For $\mathcal{L}$ cases, a single i^{th} TO, indicated by color, exhibits a distinct ω_i or K_i compared to the others, specifically $\omega_i = \delta_\omega \omega$ or $K_i = \delta_K K$. For $\mathcal{C}$ cases, half of the TOs are set to different frequencies or heater power. The term 'side-by-side' indicates that the network now consists of two mirror-asymmetric groups of TOs, a configuration also used to describe similar asymmetries in an annular combustor [60]. For $\mathcal{A}$ cases, although half of the TOs are set to different frequencies or heater power, only immediately adjacent TOs are asymmetric. When dealing with odd numbers of TOs ($n = 5, 7$) for $\mathcal{C}$ and $\mathcal{A}$ cases, the remainder TO is not set to be mismatched.

3.2.1 Frequency detuning δ_ω

We first examine the influence of δ_ω between mismatched TOs and base TOs on AD across three configurations, as represented by the $\overline{A}$ distribution. As shown in Fig. 3, the variation of $\overline{A}$ distributions is presented as a function of n for three configurations: $\mathcal{L}$, $\mathcal{C}$, and $\mathcal{A}$ (from top to bottom). $\delta_\omega = 1$ represents the uniform case where the mismatching effect does not exist. The primary findings are as follows:

(i) For $\mathcal{L}$ configuration, both increasing and decreasing δ_ω shrink the high-amplitude region and enlarge the AD region. Decreasing δ_ω achieves AD more easily with weaker coupling strength (i.e., smaller k_τ). However, as n increases, this effect diminishes. Specifically, in the case of $n = 16$, the bottom boundary of the AD region flattens. In general, the influence of localized asymmetry weakens when n increases, resulting in a more uniform distribution of $\overline{A}$ across different δ_ω values.

(ii) For $\mathcal{C}$ configuration, where half of the TOs are mismatched, increasing δ_ω induces AD more easily than decreasing δ_ω, even with relatively weak coupling strength ($k_\tau \approx 0.1$), for almost all cases. The exception occurs at $n = 5$, where only two out of five TOs are set to be mismatched. As a result, the introduced asymmetry is not strong enough,

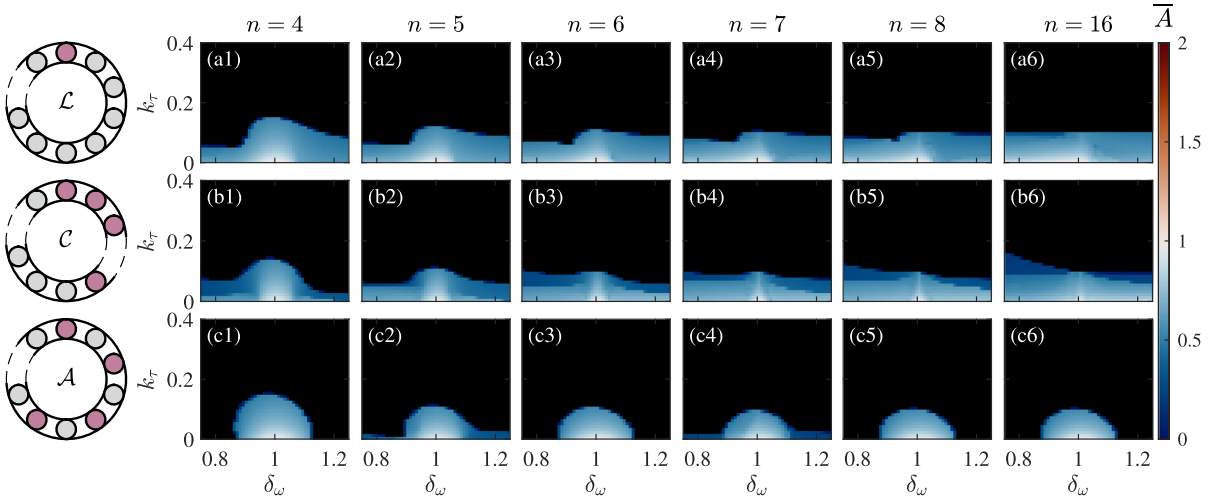

Fig. 3 Contour maps of $\overline{A}$ for three different configurations with frequency detuning. The first row is $\mathcal{L}$ configuration, second row is $\mathcal{C}$ configuration, the third row is $\mathcal{A}$ configuration. $\tau = \tau_t = 0.2$. Other parameters such as K, c_{loss}, and k_d are kept the same as in the TOs in Fig. 2

resulting in a more symmetric AD region. In the $n = 16$ case, the bottom of the AD region forms a slope when $\delta_\omega < 1$ because, as the fundamental frequency of the mismatched TOs decreases, these TOs struggle to oscillate, leading to a smaller AD region. This shows that weakened TOs do not necessarily lead to an overall suppression of oscillations, on the contrary, this can possibly less promote the emergence of AD.

(iii) For $\mathcal{A}$ configuration, the results differ significantly from the previous two. The AD region greatly expands towards lower k_τ values at both ends of the x-axis where $\delta_\omega < 0.9$ and $\delta_\omega > 1.1$. For even n cases, it is even possible to achieve AD with $k_\tau = 0$, indicating that the frequency detuning is completely dominant over the contribution from time-delay coupling to induce AD. For odd n cases, time-delay coupling is still essential for achieving AD although the AD region greatly expands to the region where k_τ can be very small. We also notice that the size of the AD region remains unaffected by n when $n \geqslant 8$.

In general, all three configurations tend to effectively promote the emergence of AD with the appropriate frequency detuning and coupling strength. However, it is also worth noting that the size of AD region first increases and then shrinks when n is larger than 5 ($\mathcal{C}$ configuration) and 6 ($\mathcal{L}$ and $\mathcal{A}$ configurations), as shown in Fig. 4. The size ratio of the AD region to the entire parameter space is denoted by η_{AD}. This implies that there exists an optimal n for three configurations to maximize the AD region. It is also encouraging to observe that $\mathcal{A}$ configuration consistently exhibits the largest AD percentage across all numbers of TOs, providing a global optimal solution for inducing AD. Meanwhile, the high-amplitude region ($\overline{A} > 0.5$) in the vicinity of the fundamental frequency ($0.9 < \delta_\omega < 1.1$) shrinks with the increase of n and no global amplitude amplification ($\overline{A} > 1$) is observed.

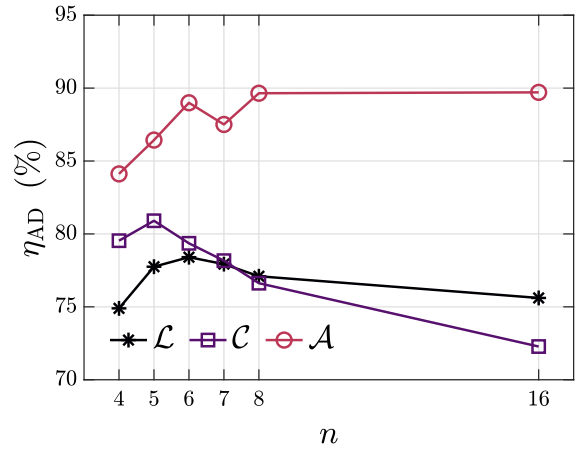

Fig. 4 The size ratio of the AD region over the entire parameter space for three different configurations presented in Fig 3

Next, we examine the non-uniform amplitude distribution among oscillators in the network by calculating the standard deviation of A_i, as illustrated in Fig. 5. Then we aim to identify the TO in this network that exhibits the highest pressure amplitude and determine its location in the parameter space defined by δ_ω and k_τ, particularly focusing on regions where σ_{A_i} is larger than 0.2. This analysis is crucial for pinpointing the primary energy source of pressure oscillations in the overall network, thus providing valuable insights for implementing control strategies that specifically target select local TOs. Such targeted control strategies can enhance effectiveness and resource efficiency by focusing on critical TOs. As shown in Fig. 6, we color the case which has the highest pressure amplitude using its corresponding color of the TO. Below is the map showing the highest pressure amplitude case. We also color the AD region in white to better delineate the region where pressure oscillation remains in the network (i.e., non-AD region). The primary findings are as follows:

(i) For $\mathcal{L}$ configuration, increasing δ_ω rather than decreasing it can lead to greater differences between the TOs. Such differences are eliminated as n increases to 16 (see Fig. 5 a6). When n is even, the primary energy to sustain the remaining pressure oscillations comes from the mismatched TO (the one wrapped with a red circle in Fig. 6 a1) or its mirrored TO. The mirrored TO becomes the primary energy source when δ_ω is significantly larger or smaller than 1 (see the yellow region in Fig. 6 b1, b3, b5, and b6). When n is odd, the primary energy comes from the mismatched TO or one of the two TOs located at both sides of the symmetric axis passing through the mismatched TO (Fig. 6 b2 and b4). This feature does not change when n increases. Such a distribution makes the overall network mirror symmetric in terms of the pressure amplitude distribution along an axis starting from the location of the global maximum of pressure amplitude to its opposite side.

(ii) For $\mathcal{C}$ configuration, when n is even, the areas where $\delta_\omega > 1$ and $\delta_\omega < 1$ have similar sizes in terms of the region where σ_{A_i} is greater than 0.2. The primary energy to sustain the remaining pressure oscillations comes from the TOs with lower natural frequency when $n = 4$ (see Fig. 6 d1). When n is odd, the differences between TOs within the region where $\delta_\omega < 1$ are significantly reduced. The primary energy come from the mismatched TO or one of the two TOs located at both sides of the symmetric axis passing through the mismatched TO (Fig. 6 d2 and d4).

(iii) For $\mathcal{A}$ configuration, our results show that one mismatched TO is strongly coupled to its adjacent uniform TO, and all the mismatched TOs have the same amplitude, as do the uniform ones. The oscillators with larger pressure amplitude are the ones with lower natural frequency in the clusters for cases of even numbers. Therefore any two adjacent TOs can be treated as a cluster (circled in dash lines), and the alternating configuration is then converted to a case with uniform clusters. The cluster is a classical two TO system coupled with frequency detuning, dissipative coupling, and time-delay coupling. This finding explains why alternating configuration shares such a large AD region and is nearly independent of n when $n > 6$.

3.2.2 Heater power mismatching δ_K

We now examine the influence of δ_K between mismatched TOs and unmodified TOs on AD for three configurations $\mathcal{L}$, $\mathcal{C}$, and $\mathcal{A}$ shown in Fig. 7 (from top to bottom). When $\delta_K > 1$, $\delta_K = 1$, and $\delta_K < 1$ the mismatched TO has a higher, equal, and lower non-dimensional heater power than that of the normal TO, respectively. The primary findings are as follows:

(i) For $\mathcal{L}$ configuration, a high-amplitude regions ($\overline{A} > 1$) emerge in the bottom right corner of the entire parameter space, indicating an amplitude amplification in that area. In this region, we also observe significant standard deviations (e.g. Figure 9 a1). The size of the high-amplitude region tends to be weakened when n increases. When $n \geqslant 8$, the amplitude amplification region almost disappears, and the size of the AD region becomes saturated, as shown in Fig. 8.

(ii) For $\mathcal{C}$ configuration, when n is small, the distribution of the amplitude ratio is similar to the $\mathcal{L}$ case (Fig. 7 b1). In the lower right corner of the parameter space, a region with amplified amplitude is also observed. Although this region diminishes as n increases, it does not completely disappear. As

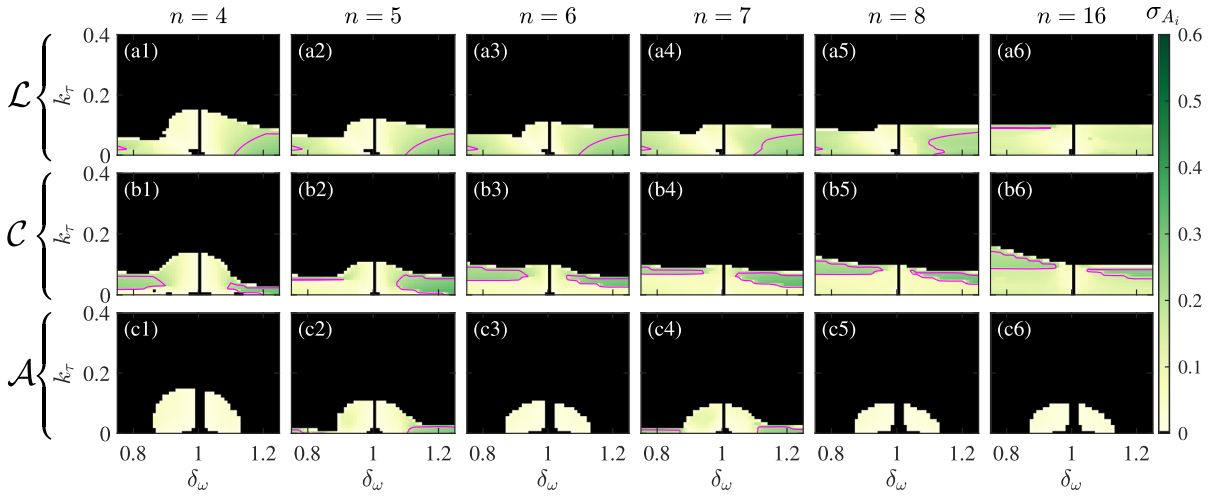

Fig. 5 The standard deviation of the normalized pressure amplitude (i.e., σ_{A_i}) with frequency detuning. Areas with $\sigma_{A_i} > 0.2$ are enclosed by magenta contour lines

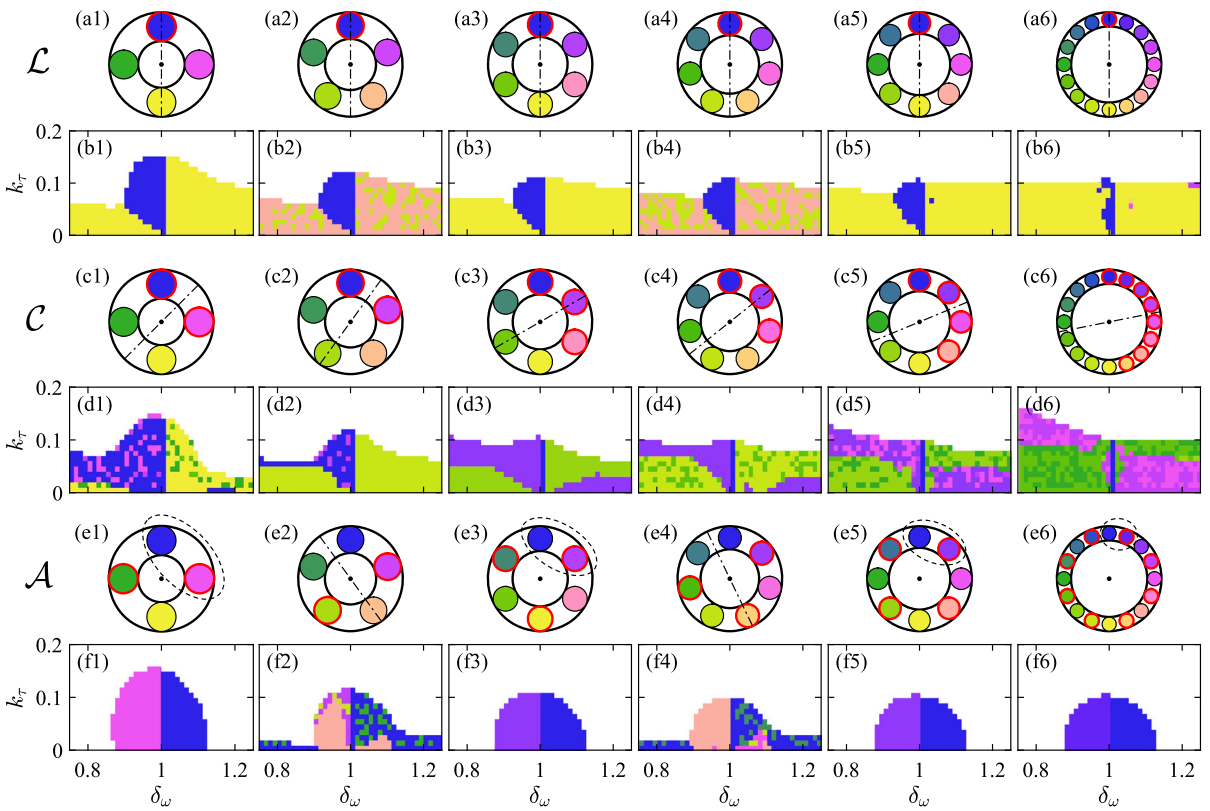

Fig. 6 Contour maps of the location where the TO with the maximum pressure amplitude is for three different configurations with frequency detuning. Different colors stand for the locations of TOs with the maximum pressure amplitude. The red circles stand for mismatched TOs. The center axes are denoted with dash-dot lines. The clusters in $\mathcal{A}$ cases are marked with dash-line circles

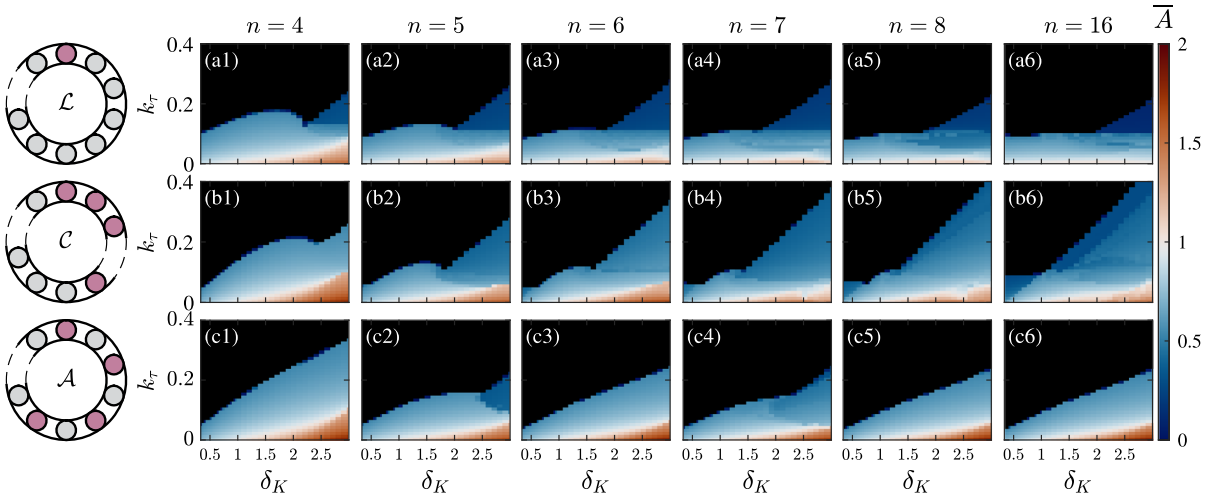

Fig. 7 Contour maps of $\overline{A}$ for three different configurations with heater power mismatching. The first row is $\mathcal{L}$ configuration, second row is $\mathcal{C}$ configuration, the third row is $\mathcal{A}$ configuration. All other parameters are kept the same as in the TOs in Fig. 2

n increases, the AD region gradually shrinks, and when $n \geqslant 8$, the AD region completely disappears when δ_K is sufficiently large (Fig. 7 b5 and b6). Both the oscillation region and the amplitude amplified region are larger in the $\mathcal{C}$ case than in the $\mathcal{L}$ case. This is possibly due to more TOs having their heater power modulated in the $\mathcal{C}$ case compared to the $\mathcal{L}$ case.

(iii) For $\mathcal{A}$ configuration, when $n = 4$, the AD region is significantly smaller compared to the $\mathcal{L}$ and $\mathcal{C}$ configurations. However, as n increases, the AD region rapidly grows and then remains constant. This pattern is also reflected in Fig. 8. In the bottom right corner of the parameter space, there is also a region of amplitude amplification, but the size of this region does not decrease as n increases. Compared to the $\mathcal{C}$ cases when $n > 4$, although the number of TOs with mismatched amplitudes is the same in both cases, the AD region in the $\mathcal{A}$ configuration does not shrink with increasing n as it does in the $\mathcal{C}$ cases. This indicates that the $\mathcal{A}$ configuration can suppress the trend of the AD region shrinking as the number of TOs with mismatched amplitude grows.

Due to the direct influence of heater power on amplitude, investigating the distribution of amplitudes in the network and identifying the location of energy sources holds greater significance. We investigated the amplitude distribution in heater power mismatching cases, as

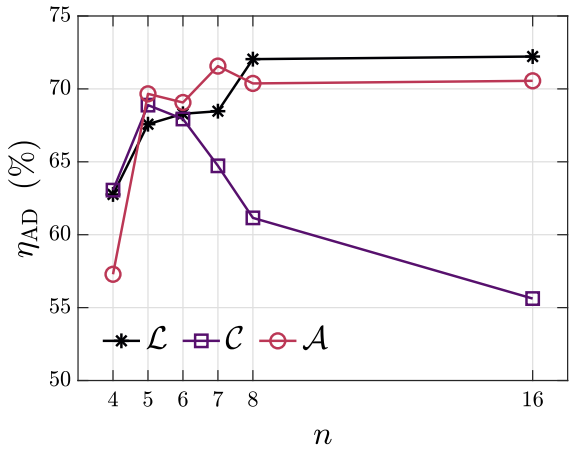

Fig. 8 The size ratio of the AD region over the entire parameter space for three different configurations presented in Fig 7

illustrated in Figs. 9 and 10. The area with $\sigma_{A_i} > 0.2$ is primarily composed of two triangular regions. One corresponds to the bottom right corner where amplitudes are relatively large, and the other is in the upper right side where k_τ is relatively large. For $\mathcal{L}$ configuration, σ_{A_i} decrease as n increases (except for $n = 8$), implying a more uniform distribution of pressure amplitude of TOs. Conversely, for $\mathcal{C}$ configuration, these differences increase with increasing n. For $\mathcal{A}$ configuration with even-numbered TOs, σ_{A_i} is smaller than other two configurations, showing a more uniform distribution of the pressure amplitude of TOs.

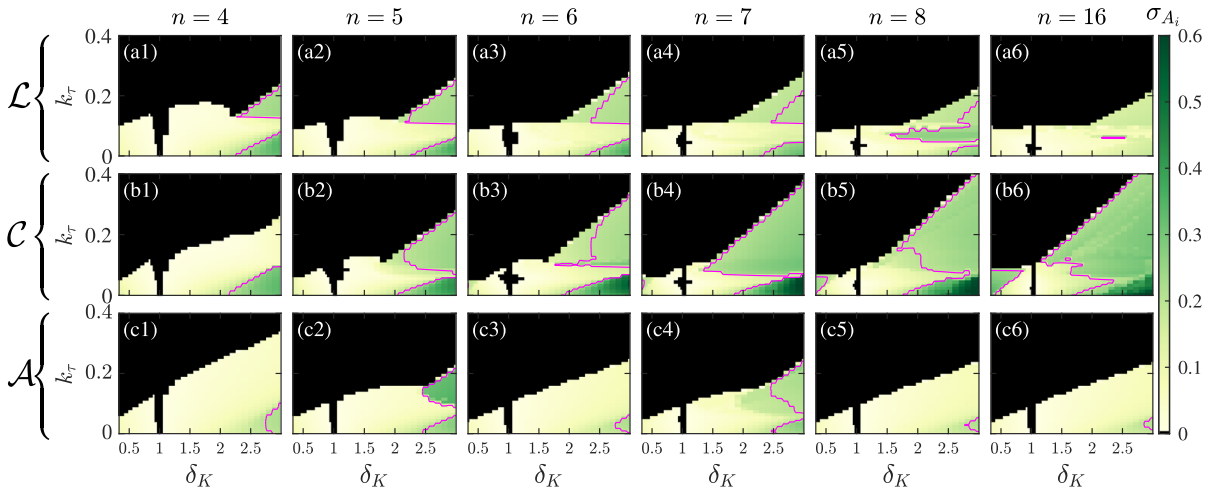

Fig. 9 The standard deviation of the normalized pressure amplitude (i.e., σ_{A_i}) with heater power mismatching. Areas with $\sigma_{A_i} > 0.2$ are enclosed by magenta contour lines

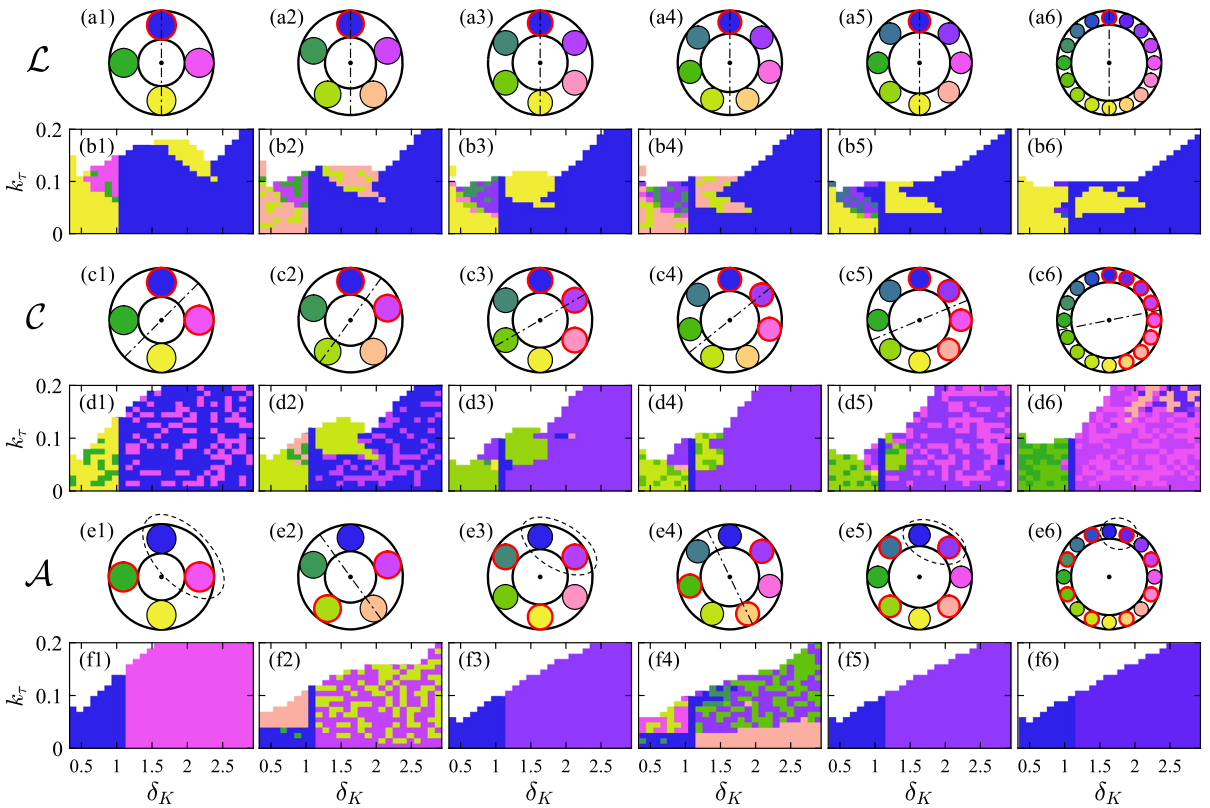

Fig. 10 Contour maps of the location where the TO with the maximum pressure amplitude is for three different configurations with heater power mismatching. Different colors stand for the locations of TOs with the maximum pressure amplitude. The red circles stand for mismatched TOs. The center axes are denoted with dash-dot lines. The clusters in $\mathcal{A}$ cases are marked with dash-line circles

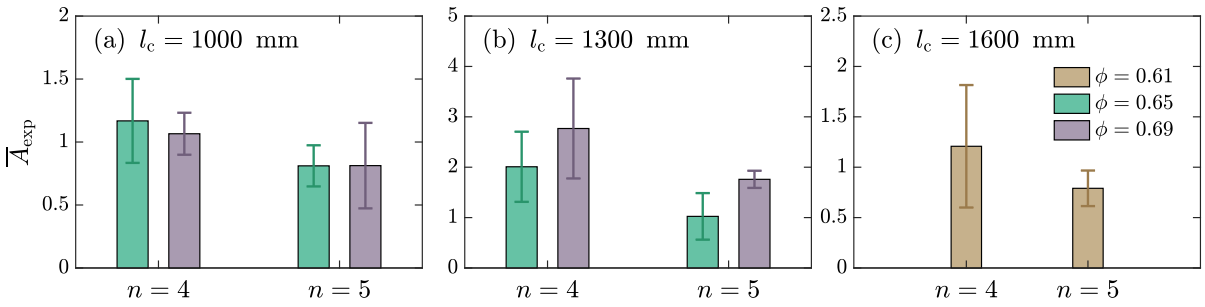

Fig. 11 Experimental results of the global average of the normalized pressure amplitude (i.e., $\overline{A}$) from 4-can and 5-can lean premixed combustors, the bar chart represents $\overline{A}$, while the error bars indicate the standard deviation of $A_{i,\mathrm{exp}}$

An interesting behavior in $\mathcal{L}$ cases is that the TO with maximum heater power is not necessarily exhibits maximum oscillation pressure amplitude. Take $n = 16$ as an example (see Fig. 10 a6), when $\delta_K = 1.5$ and $k_\tau = 0.06$, the TO with maximum amplitude is the opposite one. However, the standard deviations of these anomalous regions are relatively small, indicating that overall differences in amplitudes are not significant. Same phenomenon can also be found in $\mathcal{L}$ cases when $4 < n < 16$. But when $n = 16$, the side with larger heater power will dominate pressure amplitude distribution (see Fig. 10 d6). When k_τ is sufficiently large, we can also observe that the TOs with the maximum amplitude change from the central TOs on the mismatched side (adjacent to the symmetry axis) to the TOs at the boundary between the two sides (farthest from the symmetry axis). When $n = 4$, the network is too simple to exhibit complex amplitude distribution (see Fig. 10 d1). For $\mathcal{A}$ cases, clusters with same amplitude profile are also found in even n cases.

From the analysis above, we can conclude as follows: (1) the size of AD region is closely linked to the configuration of frequency detuning. Specifically, for $\mathcal{A}$ cases with an even n number, clusters can be found periodically exists in the ring network. Each of them is a classic two-coupled TOs system with frequency detuning, which leads to AD in the whole network. (2) Improving the heater power of typical TOs in ring coupled network can not ensure their oscillation pressure amplitudes are maximum. (3) Increasing the number of TOs can reduce the impact brought by TO asymmetry. When TOs are slightly mismatched, increasing the number of TOs tends to reduce the amplitude and expand the AD region. But when n is very large, the change is not significant.

3.3 Distribution of pressure amplitude in can-annular combustors

In this section, we investigate whether the variation of the global average of the normalized pressure amplitude (i.e., $\overline{A}$) derived from our reduced-order model above qualitatively aligns with our previous experimental observations on can-annular combustors [45–47]. Detailed descriptions of this can-annular combustion system, comprising four (i.e., 4-can) or five (i.e., 5-can) lean premixed combustors connected circumferentially with a cross-talk section, can be found in Refs. [45–47]. As shown in Fig. 11, we present the global average pressure amplitude ratio, $\overline{A}_{\mathrm{exp}} \equiv 1/n \sum_{i=1}^{n} A_{i,\mathrm{exp}}$ and the standard deviation of all TOs' pressure amplitude ratio $\sigma_{A_{i,\mathrm{exp}}}$ for different combustor lengths ($l_c = 1000$, 1300, and 1600 mm) and global equivalence ratios ($\phi = 0.61$, 0.65, and 0.69). We find that 5-can cases generally have a lower pressure amplitude and a more uniform pressure amplitude distribution than those of 4-can cases. For example, when $l_c = 1300$ mm and $\phi = 0.65$, $\overline{A}_{\mathrm{exp}}$ and $\sigma_{A_{i,\mathrm{exp}}}$ of the 5-can case are all smaller than those of the 4-can case. This agrees with our numerical observation in Sect. 3.2.2 that a network featuring a large n tends to have a stronger ability to damp energy through coupling and thus leading to a smaller global average pressure amplitude. We also find that when $l_c = 1300$ mm, $\overline{A}_{\mathrm{exp}}$ increases both for $n = 4$ and 5 when ϕ increases. In our experimental bifurcation map, we found that higher ϕ leads to a stronger TO featured with higher pressure amplitude. The non-dimensional heater power K has an analogous role in determining the pressure amplitude in our numerical study. So when we increase δ_K for $\mathcal{C}$ and $\mathcal{A}$, half of the total TOs become stronger, lead-

ing to a larger $\overline{A}$. This feature is well captured in Fig. 7 that a blue ramp ($\overline{A} \approx 0.4$) emerges when $\delta_K > 1$.

In a quick summary, the qualitative agreement in terms of the pressure amplitude variation across different numbers of TOs between the proposed reduced-order model and experimental results implies that the numerical results presented in Sect. 3.2.1 and 3.2.2 could be potentially used to help the design of passive control strategies by introducing asymmetries into a multi-combustor system. For instance, adding baffles not only increases damping but also induces slight frequency shifts in the combustion chamber [61]. However, in can-annular combustors, effective control may not require installing baffles in every chamber. Instead, implementing an $\mathcal{A}$ configuration, where baffles are alternately installed in selected chambers, significantly increases the likelihood of achieving amplitude death.

4 Conclusions

In this study, we numerically investigate a ring-coupled network consisting of nonlocally coupled asymmetric thermoacoustic oscillators, with a focus on the influence of the network size (up to 16) and three asymmetry configurations on the emergence of amplitude death. For three asymmetry configurations, named localized $\mathcal{L}$, 'side-by-side' $\mathcal{C}$, and alternating $\mathcal{A}$, we introduce the asymmetry to them by tuning thermoacoustic oscillator's frequency and mismatching thermoacoustic oscillator's heater power, respectively. Our answers to the three research questions raised in Sect. 1 can be summarized as follows.

(i) Using the nonlocal time-delay coupling network model proposed in this study, we find the amplitude distribution numerically predicted when varying the number of TOs (n) and heater power (K) qualitatively agree with the experimental observations [45–47] when varying the number of cans and equivalence ratio.

(ii) The AD region will be first enlarged when the number of TOs increases to a moderately large number ($n = 5$ or 6) for all three asymmetric configurations. With frequency detuning, the AD region shrinks for $\mathcal{L}$ and $\mathcal{C}$ configurations as n increases to a larger number (up to 16). In contrast, the AD region remains unaffected for the $\mathcal{A}$ configuration, consistently larger than the other two configurations across all values of n, making it an optimal choice for inducing amplitude death in a ring-coupled network. When heater power mismatching is applied, shrinking only appears in $\mathcal{C}$ cases. The AD region remains unchanged for $\mathcal{L}$ and $\mathcal{A}$ configurations when n increases to 16.

(iii) The $\mathcal{A}$ configurations with frequency detuning promote the emergence of AD the most, particularly when the frequency detuning is large (i.e., $\delta_\omega > 1.1$ or $\delta_\omega < 0.9$). Across varying numbers of thermoacoustic oscillators, $\mathcal{A}$ consistently yields a larger AD region. Compared to the $\mathcal{C}$ configuration, this observation also applies to the heater power mismatching cases when $n > 4$, despite both configurations having the same number of oscillators with amplified power. The oscillator with the highest pressure amplitude often locates at the mismatched side or its opposite side, with the center axis passing through it. For the $\mathcal{A}$ configuration, such an oscillator exists with its neighbouring base oscillator (not mismatched) in a pair.

The implications of this study are twofold. First, along with our previous low-order modeling studies [39,40], we confirm the feasibility of using the reduced-order model to qualitatively predict system dynamical behavior, particularly amplitude death. This approach can assist in designing passive control strategies for thermoacoustic oscillations. By identifying the oscillator with the highest pressure amplitude, we can apply previously developed control strategies [62–66] to further weaken the remaining oscillations in the network. Second, recent experimental studies on symmetry breaking in annular combustors indicate that thermoacoustic oscillations can be weakened by introducing asymmetries into the combustion system [60]. Our numerical study further confirms this, suggesting new possibilities for using mismatched thermoacoustic oscillators to induce amplitude death and thus globally weaken thermoacoustic oscillations in multi-combustor systems. However, the findings are based on simplified assumptions, such as the heat release model and uniform coupling conditions, which can not fully represent real-world combustor systems. Future work will extend the current framework by incorporating alternative source term models, such as the n–τ model or hybrid approaches that integrate CFD to better

resolve flame dynamics [67] for a more comprehensive understanding.

Funding Open access funding provided by The Hong Kong Polytechnic University LZ, YL and YG were supported by the National Natural Science Foundation of China (Grant No. 52306166). KTK was supported by the Korea Institute of Energy Technology Evaluation and Planning (KETEP) and the Ministry of Trade, Industry & Energy (MOTIE) of the Republic of Korea (Grant # RS-2023-00270080, Development of a Method for Testing and Evaluating Hydrogen Turbine Combustor). JZ was supported by the National Natural Science Foundation of China (Grant No. 12072277).

Data Availability The data that support the findings of this study are available upon reasonable request.

Declarations

Conflict of interest The authors declare that they have no conflict of interest.

Appendix A Bifurcation diagram

We validate the bifurcation behavior of a single uncoupled thermoacoustic TO. We numerically solve the ODEs in Eqs. (10–12). The pressure and velocity is measured at $x = 0.5$. The results are shown in Fig. 12. The forward process is calculated with the same initial value at discrete heater power K, while the backward process is calculated base on continuing time history with K discretely varying. Figure 12a and b are the time history and limited cycle frequency of pressure oscillation at $K = 0.7$. Hysteresis of heater power is observed between forward and backward process, as shown in Fig. 12. The Hopf point is $K = 0.64$ and the saddle point is $K = 0.53$.

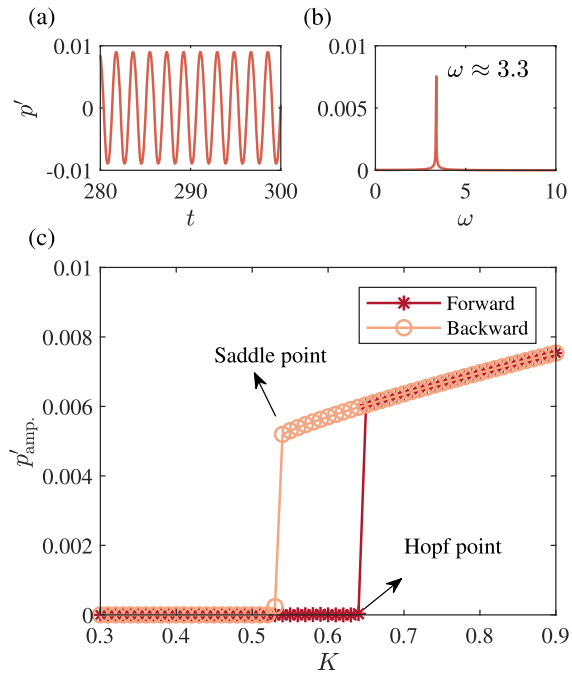

Fig. 12 Characteristic of a single uncoupled TO, **a** time history of the pressure oscillation p' at $K = 0.7$, **b** the corresponding FFT analysis and **c** pressure amplitude $p'_{\text{amp.}}$ as a function of the nondimensional heater power K

References

1. McManus, K., Poinsot, T., Candel, S.M.: A review of active control of combustion instabilities. Prog. Energy Combust. Sci. **19**(1), 1–29 (1993)
2. Poinsot, T.: Prediction and control of combustion instabilities in real engines. Proc. Combust. Inst. **36**(1), 1–28 (2017)
3. Zhao, D., Lu, Z., Zhao, H., Li, X., Wang, B., Liu, P.: A review of active control approaches in stabilizing combustion systems in aerospace industry. Prog. Aerosp. Sci. **97**, 35–60 (2018)
4. Huang, Y., Yang, V.: Dynamics and stability of lean-premixed swirl-stabilized combustion. Prog. Energy Combust. Sci. **35**(4), 293–364 (2009)
5. Sirignano, W.A.: Driving mechanisms for combustion instability. Combust. Sci. Technol. **187**(1–2), 162–205 (2015)
6. O'Connor, J.: Understanding the role of flow dynamics in thermoacoustic combustion instability. Proc. Combust. Inst. **39**(4), 4583–4610 (2023)
7. Bethke, S., Krebs, W., Flohr, P., Prade, B.: Thermoacoustic properties of can annular combustors. In: 8th AIAA/CEAS Aeroacoustics Conference and Exhibit, p. 2570 (2002)
8. Kaufmann, P., Krebs, W., Valdes, R., Wever, U.: 3D thermoacoustic properties of single can and multi can combustor configurations. In: Turbo Expo: Power for Land, Sea, and Air, vol. 43130, pp. 527–538 (2008)

9. Ghirardo, G., Di Giovine, C., Moeck, J., Bothien, M.: Thermoacoustics of can-annular combustors. J. Eng. Gas Turbines Power **141**(1), 011007 (2019)
10. Buschmann, P., Worth, N., Moeck, J.: Thermoacoustic oscillations in a can-annular model combustor with asymmetries in the can-to-can coupling. Proc. Combust. Inst. **39**(4), 5707–5715 (2023)
11. Orchini, A., Moeck, J.P.: Weakly nonlinear analysis of thermoacoustic oscillations in can-annular combustors. J. Fluid Mech. **980**, 52 (2024)
12. Saxena, G., Prasad, A., Ramaswamy, R.: Amplitude death: the emergence of stationarity in coupled nonlinear systems. Phys. Rep. **521**(5), 205–228 (2012)
13. Raaj, A., Mondal, S., Jagdish, V.: Investigating amplitude death in a coupled nonlinear aeroelastic system. Int. J. Non-Linear Mech. **129**, 103659 (2021)
14. Kuntsevich, B., Pisarchik, A.: Synchronization effects in a dual-wavelength class-B laser with modulated losses. Phys. Rev. E **64**(4), 046221 (2001)
15. Manoj, K., Pawar, S., Sujith, R.: Experimental evidence of amplitude death and phase-flip bifurcation between in-phase and anti-phase synchronization. Sci. Rep. **8**(1), 11626 (2018)
16. Reddy, D., Sen, A., Johnston, G.: Time delay induced death in coupled limit cycle oscillators. Phys. Rev. Lett. **80**(23), 5109 (1998)
17. Dodla, R., Sen, A., Johnston, G.: Phase-locked patterns and amplitude death in a ring of delay-coupled limit cycle oscillators. Phys. Rev. E **69**(5), 056217 (2004)
18. Kengne, R., Tchitnga, R., Mabekou, S., Tekam, B., Soh, G., Fomethe, A.: On the relay coupling of three fractional-order oscillators with time-delay consideration: Global and cluster synchronizations. Chaos Solitons Fract. **111**, 6–17 (2018)
19. Sugitani, Y., Konishi, K.: Amplitude death in delay-coupled oscillators on directed graphs. Phys. Rev. E **105**(6), 064202 (2022)
20. Mirollo, R., Strogatz, S.: Amplitude death in an array of limit-cycle oscillators. J. Stat. Phys. **60**, 245–262 (1990)
21. Aronson, D., Ermentrout, G., Kopell, N.: Amplitude response of coupled oscillators. Physica D **41**(3), 403–449 (1990)
22. Prasad, A.: Universal occurrence of mixed-synchronization in counter-rotating nonlinear coupled oscillators. Chaos Solitons Fract. **43**(1–12), 42–46 (2010)
23. Mizukami, S., Konishi, K., Sugitani, Y., Kouda, T., Hara, N.: Effects of frequency mismatch on amplitude death in delay-coupled oscillators. Phys. Rev. E **104**(5), 054207 (2021)
24. Sharma, A., Suresh, K., Thamilmaran, K., Prasad, A., Shrimali, M.: Effect of parameter mismatch and time delay interaction on density-induced amplitude death in coupled nonlinear oscillators. Nonlinear Dyn. **76**, 1797–1806 (2014)
25. Hou, Z., Xin, H.: Oscillator death on small-world networks. Phys. Rev. E **68**(5), 055103 (2003)
26. Konishi, K., Yoshida, K., Sugitani, Y., Hara, N.: Delay-induced amplitude death in multiplex oscillator network with frequency-mismatched layers. Phys. Rev. E **109**(1), 014220 (2024)
27. Biju, A., Srikanth, S., Manoj, K., Pawar, S., Sujith, R.: Dynamics of minimal networks of limit cycle oscillators. Nonlinear Dyn. **112**, 1–20 (2024)
28. Biwa, T., Tozuka, S., Yazaki, T.: Amplitude death in coupled thermoacoustic oscillators. Phys. Rev. Appl. **3**(3), 034006 (2015)
29. Delage, R., Takayama, Y., Biwa, T.: Bifurcation diagram of coupled thermoacoustic chaotic oscillators. Chaos **28**(8), 083125 (2018)
30. Hyodo, H., Biwa, T.: Stabilization of thermoacoustic oscillators by delay coupling. Phys. Rev. E **98**(5), 052223 (2018)
31. Saldern, J., Orchini, A., Moeck, J.: Analysis of thermoacoustic modes in can-annular combustors using effective Bloch-type boundary conditions. J. Eng. Gas Turbines Power **143**(7), 071019 (2021)
32. Humbert, S., Orchini, A.: Acoustics of can-annular combustors: Experimental characterisation and modelling of a lab-scale multi-can setup with adjustable geometry. J. Sound Vib. **564**, 117864 (2023)
33. Dange, S., Manoj, K., Banerjee, S., Pawar, S., Mondal, S., Sujith, R.: Oscillation quenching and phase-flip bifurcation in coupled thermoacoustic systems. Chaos **29**(9), 093135 (2019)
34. Hyodo, H., Iwasaki, M., Biwa, T.: Suppression of Rijke tube oscillations by delay coupling. J. Appl. Phys. **128**(9), 094902 (2020)
35. Jegal, H., Moon, K., Gu, J., Li, L., Kim, K.: Mutual synchronization of two lean-premixed gas turbine combustors: phase locking and amplitude death. Combust. Flame **206**, 424–437 (2019)
36. Moon, K., Guan, Y., Li, L., Kim, K.: Mutual synchronization of two flame-driven thermoacoustic oscillators: dissipative and time-delayed coupling effects. Chaos **30**(2), 023110 (2020)
37. Guan, Y., Moon, K., Kim, K., Li, L.: Synchronization and chimeras in a network of four ring-coupled thermoacoustic oscillators. J. Fluid Mech. **938**, 5 (2022)
38. Guan, Y., Li, L., Jegal, H., Kim, K.: Effect of flame response asymmetries on the modal patterns and collective states of a can-annular lean-premixed combustion system. Proc. Combust. Inst. **39**(4), 4731–4739 (2023)
39. Guan, Y., Moon, K., Kim, K., Li, L.: Low-order modeling of the mutual synchronization between two turbulent thermoacoustic oscillators. Phys. Rev. E **104**(2), 024216 (2021)
40. Liao, Y., Guan, Y., Liu, P., Moon, K., Kim, K.: Low-order modeling of collective dynamics of four ring-coupled turbulent thermoacoustic oscillators. Nonlinear Dyn. **112**, 6897–6917 (2024)
41. Zhang, H., Xu, D., Lu, C., Qi, E., Hu, J., Wu, Y.: Amplitude death of a multi-module floating airport. Nonlinear Dyn. **79**, 2385–2394 (2015)
42. Zou, W., Senthilkumar, D., Zhan, M., Kurths, J.: Quenching, aging, and reviving in coupled dynamical networks. Phys. Rep. **931**, 1–72 (2021)
43. Pedergnana, T., Noiray, N.: Coupling-induced instability in a ring of thermoacoustic oscillators. Proc. R. Soc. A **478**(2259), 20210851 (2022)
44. Orchini, A., Pedergnana, T., Buschmann, P., Moeck, J., Noiray, N.: Reduced-order modelling of thermoacoustic instabilities in can-annular combustors. J. Sound Vib. **526**, 116808 (2022)
45. Moon, K., Jegal, H., Yoon, C., Kim, K.: Cross-talk-interaction-induced combustion instabilities in a can-

annular lean-premixed combustor configuration. Combust. Flame **220**, 178–188 (2020)
46. Moon, K., Yoon, C., Kim, K.: Influence of rotational asymmetry on thermoacoustic instabilities in a can-annular lean-premixed combustor. Combust. Flame **223**, 295–306 (2021)
47. Moon, K., Bae, D., Kim, K.: Modal dynamics of self-excited thermoacoustic instabilities in even and odd numbered networks of lean-premixed combustors. Combust. Flame **255**, 112928 (2023)
48. Matveev, K., Culick, F.: A study of the transition to instability in a Rijke tube with axial temperature gradient. J. Sound Vib. **264**(3), 689–706 (2003)
49. Juniper, M.: Triggering in the horizontal Rijke tube: non-normality, transient growth and bypass transition. J. Fluid Mech. **667**, 272–308 (2011)
50. Magri, L., Juniper, M.: Sensitivity analysis of a time-delayed thermo-acoustic system via an adjoint-based approach. J. Fluid Mech. **719**, 183–202 (2013)
51. Sayadi, T., Le Chenadec, V., Schmid, P., Richecoeur, F., Massot, M.: Thermoacoustic instability – a dynamical system and time domain analysis. J. Fluid Mech. **753**, 448–471 (2014)
52. Fournier, G., Schaefer, F., Haeringer, M., Silva, C., Polifke, W.: Interplay of clusters of acoustic and intrinsic thermoacoustic modes in can-annular combustors. J. Eng. Gas Turbines Power **144**(12), 121015 (2022)
53. Li, X., Xu, B., Li, X., Pang, K., Li, X., Zhang, H.: Effects of multiplicative and additive colored noises on the stability of a simplified thermoacoustic combustor. Combust. Flame **249**, 112413 (2023)
54. Heckl, M.: Non-linear acoustic effects in the Rijke tube. Acta Acust. united Acust. **72**(1), 63–71 (1990)
55. Zinn, B., Lores, M.: Application of the Galerkin method in the solution of non-linear axial combustion instability problems in liquid rockets. Combust. Sci. Technol. **4**(1), 269–278 (1971)
56. Balasubramanian, K., Sujith, R.: Thermoacoustic instability in a Rijke tube: non-normality and nonlinearity. Phys. Fluids **20**(4), 044103 (2008)
57. Matveev, K.: Thermoacoustic Instabilities in the Rijke Tube: Experiments and Modeling. California Institute of Technology, United States (2003)
58. Thomas, N., Mondal, S., Pawar, S., Sujith, R.: Effect of time-delay and dissipative coupling on amplitude death in coupled thermoacoustic oscillators. Chaos **28**(3), 033119 (2018)
59. Vathakkattil Joseph, G., Pakrashi, V.: Limits on anti-phase synchronization in oscillator networks. Sci. Rep. **10**(1), 10178 (2020)
60. Latour, V., Durox, D., Renaud, A., Candel, S.: Experiments on symmetry breaking of azimuthal combustion instabilities and their analysis combining acoustic energy balance and flame describing functions. J. Fluid Mech. **985**, 31 (2024)
61. Salarvand, Hamid: Shateri, Ali Reza, Nadooshan, Afshin Ahmadi, Karimipour, Iman: Numerical study of the effect of the corrugated baffle on the acoustic characteristics of the combustion chamber. Acta Acust. **6**, 33 (2022)
62. Guan, Y., Gupta, V., Kashinath, K., Li, L.K.: Open-loop control of periodic thermoacoustic oscillations: experiments and low-order modelling in a synchronization framework. Proc. Combust. Inst. **37**(4), 5315–5323 (2019)
63. Guan, Y., He, W., Murugesan, M., Li, Q., Liu, P., Li, L.K.: Control of self-excited thermoacoustic oscillations using transient forcing, hysteresis and mode switching. Combust. Flame **202**, 262–275 (2019)
64. Roy, A., Mondal, S., Pawar, S.A., Sujith, R.: On the mechanism of open-loop control of thermoacoustic instability in a laminar premixed combustor. J. Fluid Mech. **884**, 2 (2020)
65. Zhang, M., Li, J., Cheng, W., Li, T.: Active control of thermoacoustic instability using microsecond plasma discharge. J. Appl. Phys. **127**(3), 033301 (2020)
66. Ghani, A., Polifke, W.: Control of intrinsic thermoacoustic instabilities using hydrogen fuel. Proc. Combust. Inst. **38**(4), 6077–6084 (2021)
67. Jaensch, S., Merk, M., Gopalakrishnan, E., Bomberg, S., Emmert, T., Sujith, R., Polifke, W.: Hybrid CFD/low-order modeling of nonlinear thermoacoustic oscillations. Proc. Combust. Inst. **36**(3), 3827–3834 (2017)